J Mater Sci (2010) 45:1107–1116
DOI 10.1007/s10853-009-4053-z

Electrical and thermal conductivities of porous $SiC/SiO_2/C$ composites with different morphology from carbonized wood

Joko Sulistyo · Toshimitsu Hata · Hiroyuki Kitagawa · Paul Bronsveld · Masashi Fujisawa · Kozo Hashimoto · Yuji Imamura

Received: 27 May 2009 / Accepted: 18 November 2009 / Published online: 3 December 2009

Abstract Porous $SiC/SiO_2/C$ composites exhibiting a wide range of high thermal and electrical conductivities were developed from carbonized wood infiltrated with SiO_2. As a pre-treatment, the samples were either heated at 100 °C or kept at room temperature followed by sintering in the temperature range 1200–1800 °C. The microstructure, the morphology, and the electrical and thermal conductivities of the composites were investigated. Pre-treatment at room temperature followed by sintering up to 1800 °C produced composites exhibiting a greater size of carbon crystallites, a higher ordering of the microstructure of carbon and β-SiC and a smaller amount of SiO_2, resulting in electrical and thermal conductivities of $1.17 \times 10^4\ \Omega^{-1}\ m^{-1}$ and 25 W/mK, respectively. The thermal conductivity could be further improved to 101 W/mK by increasing the density of the composite to 1.82 g/cm^3. In contrast, the pre-treatment at 100 °C produced composites possessing a lower thermal conductivity of 2 W/mK.

J. Sulistyo · T. Hata (✉) · Y. Imamura
Laboratory of Innovative Humano-habitability, Research Institute for Sustainable Humanosphere, Kyoto University, Uji Campus, Gokasho, Uji, Kyoto 611-0011, Japan
e-mail: hata@rish.kyoto-u.ac.jp

J. Sulistyo
Department of Forest Products Technology, Faculty of Forestry, Gadjah Mada University, Jl Agro No.1, Bulaksumur, Yogyakarta 55281, Indonesia

H. Kitagawa
Department of Materials Science, Shimane University, Nishikawatsu 1060, Matsue, Shimane 690-8504, Japan

P. Bronsveld
Deparment of Applied Physics, University of Groningen, Groningen, The Netherlands

M. Fujisawa
Institute of Wood Technology, Akita Prefectural University, 11-1 Kaieizaka Nosiro, Akita 016-0876, Japan

K. Hashimoto
Laboratory of Applied Radio Engineering for Humanosphere, Research Institute for Sustainable Humanosphere, Kyoto University, Uji Campus, Gokasho, Uji, Kyoto 611-0011, Japan

Introduction

Carbonized wood is an important material possessing a variety of properties and functions that depend on the carbonization process or heat treatment conditions. The microstructure and pore structure of carbonized wood are determined by heat treatments. The predominant structure is turbostratic [1] with pores existing between the elementary graphite crystals [2]. The porous structure in carbonized wood plays an important role in the infiltration of liquid and gas phase chemicals during manufacturing engineering materials such as lignocelluloses ceramics.

In recent years, the reaction of carbonized wood with SiO_2 to generate silicon carbide (SiC) has attracted much interest [3–6], motivated by the fact that carbonized wood is a natural material and the production of SiC does not involve very high temperatures. SiC exhibits high strength, good thermal conductivity, heat-resistance, and low density ($\sim$2.3 g/cm^3). It has been widely used in applications ranging from high power electronics to lightweight spacecraft components [7, 8]. Considering its manufacturing process and thermal properties, SiC composites produced from carbonized wood are potential candidates for thermal conductive applications in solar power satellites (SPS).

Some common methods used to convert carbonized wood into SiC are solid–solid reaction [4], gas phase infiltration [5], liquid phase infiltration [7], and sol–gel method [9]. Although a solid–solid reaction in a mixture of SiO_2 powder and carbonized wood is a simple and convenient method, it is difficult to obtain a uniform distribution of SiO_2, which leads to a lack of uniformity of SiC in the resulting composite. In the sol–gel method, SiO_2 liquid is infiltrated into carbonized wood in vacuum followed by a heat treatment at 100 °C. SiC crystals are uniformly distributed during sintering in a gas–solid reaction.

In this study, a simple method was developed to convert carbonized wood into SiC by infiltration of ethylsilicate-40 followed by a pre-treatment step, involving heating at 100 °C or maintaining the sample at room temperature, to cause the SiO_2 to be in a liquid or solid phase, respectively. These pre-treatments caused gas–solid and solid–solid reactions to occur during sintering, resulting in $SiC/SiO_2/C$ composites with different electrical and thermal conductivities. The effect of these pre-treatment methods on the crystal structure, the morphology, and the electrical and thermal conductivities of the composites was investigated. The structure and morphology were analyzed by X-ray diffraction, Raman spectroscopy, and scanning electron microscopy. Chemical bond analysis on the composite was made by X-ray photoelectron spectroscopy. The electrical and thermal conductivities were measured by a four-probe-method and a laser flash method, respectively.

Experimental procedure

Sugi (*Cryptomeria japonica*) wood particles were heated at a rate of 4 °C/min up to 700 °C in a laboratory scale electric furnace. The particles were held at 700 °C for 1 h under a N_2 gas flow of 100 mL/min. The resulting carbonized wood was then granulated using a blender and sieved to yield particle sizes of 45–150 μm. A silica solution was prepared by diluting ethylsilicate-40 (Colcoat, Japan) with ethyl alcohol to obtain a 15% SiO_2 concentration by weight. The carbonized wood was submerged in the silica solution and held under a vacuum of 1 kPa for 90 min. In order to produce morphological differences in the $SiC/SiO_2/C$ composite, some of the carbonized wood infiltrated with ethylsilicate-40 were heat-treated at 100 °C in an electric oven (denoted as HT100), and some were simply kept at room temperature until it dried (denoted as NHT). The final SiO_2 content calculated by the molar ratio was found to be 50% based on the dry charcoal weight. A dry weight of 1 g of carbonized wood infiltrated with SiO_2 was then placed into a 10 mm-internal-diameter graphite die with a length of 5 cm equipped with two graphite punches with a total length of 4.5 cm. Graphite punches with a total length of 5 cm were used to obtain higher density porous $SiC/SiO_2/C$ composites. To evaluate the effect of sintering temperature, porous $SiC/SiO_2/C$ composites prepared with HT100 and NHT, hereafter denoted as $SiC/SiO_2/C$ (HT100) and $SiC/SiO_2/C$ (NHT), were heated to 1200, 1400, 1600, and 1800 °C at a rate of 250 °C/min with a holding time of 30 min under a pressure of 15 MPa and a N_2 gas flow of 1 L/min using a pulse current sintering device (VCSP II, SS Alloy, Hiroshima). The 5-mm-thickness samples obtained were cut into discs with a thickness of approximately 0.8 mm.

X-ray diffraction (XRD, Rigaku-RINT-ultra X18) at 45 kV and 200 mA was used to determine the crystalline phase formed during sintering. The data were collected as continuous scans, with a step size of 0.02° 2θ and a scan rate of 1° 2θ/min between 10 and 90° 2θ. The bulk samples were analyzed without powdering since a random orientation of crystallites was assumed to be already present [10]. The full-width at half-maximum (FWHM) data and peak angles of the {002} and {100} were used in the Scherrer equation to determine the average crystallite thickness and diameter [11]

$$t = \frac{\kappa \lambda}{(B \cos \theta)} \quad (1)$$

where t is the crystallite dimension, λ is the XRD wavelength, 2θ is the scattering angle (in radians), B is the FWHM (in radians of theta), and κ is a constant. For the turbostratic crystallites as dimension perpendicular to the graphene sheets (L_c), {002} data were used with κ equals to 0.9, while for the in-plane dimension (L_a), {100} data were used with κ equals to 1.84.

The microstructure of the samples was analyzed using Raman spectroscopy (Renishaw inVia) with an air-cooled CCD detector. An argon laser with a wavelength of 514.5 nm was used as an excitation source. The spectra were measured in the 600–1,800 cm^{-1} range. Seven 10-s accumulations were collected to give an adequate signal-to-noise ratio. The wave number was calibrated using the 520 cm^{-1} line of a silicon wafer. Spectral processing was performed using WiRE 2 software.

The chemical composition analysis was performed using X-ray photoelectron spectroscopy (XPS, Shimadzu/Kratos). The samples were placed on double-sided adhesive-carbon tape mounted on a sample holder. XPS spectra were obtained using non-monochromatic MgKα radiation (1,253.6 eV), the source of which was operated at 15 kV and 10 mA. The vacuum pressure during analysis was lower than 2.0×10^{-7} Pa. High resolution scans were performed at 40 eV pass energy for the C-1s, O-1s, and Si-2p spectra. The binding energy scale was corrected by referring to the polyaromatic peak in the C-1s spectrum being 284.6 eV.

Shirley was subtracted from the C-1s, O-1s, and Si-2p spectra. The Gaussian–Lorentzian mode function was used for curve fitting of the spectra.

The morphology of the composites was observed using scanning electron microscopy (SEM, JEOL-JSM-5310). The samples were observed directly without any coating. Transmission electron microscopy (TEM, JEOL-JEM-2100F), equipped with electron energy-loss spectroscopy (EELS, GATAN) was performed to observe the microstructure and chemical composition on a $SiC/SiO_2/C$ (HT100) sample sintered at 1600 °C. Thin samples for TEM were prepared by a SEM–FIB (JEOL-JIB4500). Tungsten was used to protect the surface of the sample, and a 30 kV Ga ion beam was used in the preparation of the thin sample.

The electrical conductivity at room temperature was measured by a four-probe-method (Loresta HP MCP-T410). The thermal diffusivity (α) and the specific heat (C_p) were measured at room temperature by the laser flash method using a thermal constant analyzer (Ulvac, TC-7000H). The thermal conductivity (K_T) was calculated by the following equation:

$$K_T = \rho C_p \alpha \quad (2)$$

where ρ is the bulk density of the specimen (g/cm^3), C_p is specific heat ((J/g)/K), and α is the thermal diffusivity (m^2/s).

Results and discussion

The XRD patterns of porous $SiC/SiO_2/C$ (HT100) and $SiC/SiO_2/C$ (NHT) prepared at different sintering temperatures are shown in Fig. 1a, b. Major diffraction peaks are observed at around $2\theta = 14$ and 17°, corresponding to the SiO_2 crystal phase, around $2\theta = 26$, 44, and 79°, corresponding to the (002), (101), and (110) turbostratic carbon phase, respectively, and around $2\theta = 35$, 42, 60, and 72°, corresponding to the (111), (200), (220), and (311) reflections of the cubic β-SiC phase [12–14]. The shoulder on the (111) reflection is associated with stacking faults (labeled sf) [15]. The intensity of the β-SiC peaks both in the $SiC/SiO_2/C$ (HT100) and $SiC/SiO_2/C$ (NHT) samples showed little dependence on sintering temperature. In the case of $SiC/SiO_2/C$ (NHT) composite, a large β-SiC peak was found at sintering temperature of 1400 °C.

Figure 2a, b shows carbon structural changes in the composites as a function of sintering temperature. Both the crystallite mean layer diameter (L_a) and height (L_c) increased as the sintering temperature was increased. Moreover, L_a and L_c were found to be larger in the $SiC/SiO_2/C$ (NHT) composites than in the $SiC/SiO_2/C$ (HT100) composites. This is an interesting finding, and may possibly be explained by the presence of liquid and solid SiO_2

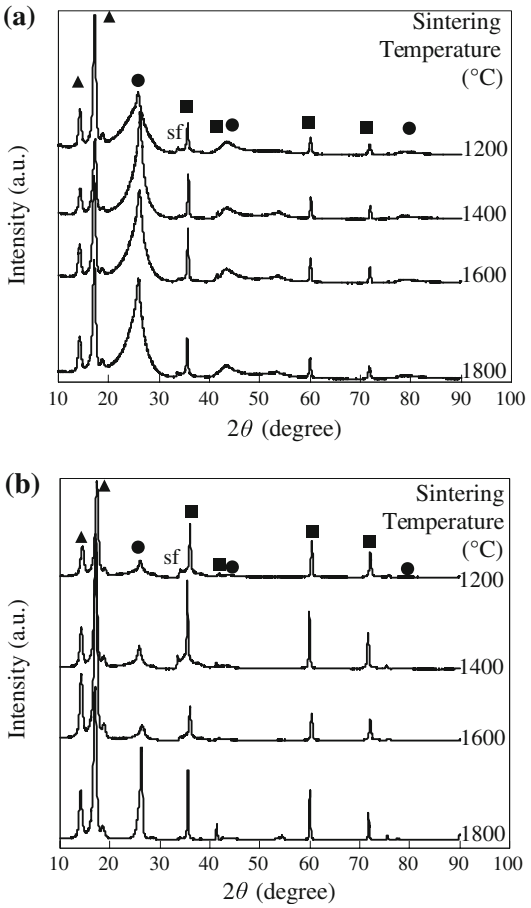

Fig. 1 X-ray diffraction patterns of porous $SiC/SiO_2/C$ composites prepared by **a** HT100 and **b** NHT at different sintering temperatures. (●) C, (■) β-SiC, (▲) SiO_2. *Note*: $SiC/SiO_2/C$ (HT100), $SiC/SiO_2/C$ prepared by a heat treatment of carbonized wood infiltrated with ethylsilicate-40 at 100 °C; $SiC/SiO_2/C$ (NHT), $SiC/SiO_2/C$ prepared with no heat treatment by keeping carbonized wood infiltrated with ethylsilicate-40 at room temperature

phases in the $SiC/SiO_2/C$ (HT100) and $SiC/SiO_2/C$ (NHT) composites, respectively. During sintering of the $SiC/SiO_2/C$ (HT100) composite, SiO_2 (liquid) reacts with carbonized wood to generate SiO gas, which then infiltrates the wood to form β-SiC. It is believed that the presence of β-SiC in the interior of the wood may suppress the growth of carbon crystallites. In the case of the $SiC/SiO_2/C$ (NHT) composite, the SiO_2 (solid) reacts with carbonized wood to produce β-SiC only at the interface. Therefore, during sintering, larger carbon crystallites can be formed in the inner regions of carbonized wood particles. The increase of L_a and L_c may be due to an increased average number of graphene sheets per turbostratic crystallite or a narrower distribution of graphene sheet spacing [16].

Figure 3a shows Raman spectra where a single peak appears at around 783–794 cm^{-1}, corresponding to the transverse optic (TO) phonon mode of cubic β-SiC [8, 17,

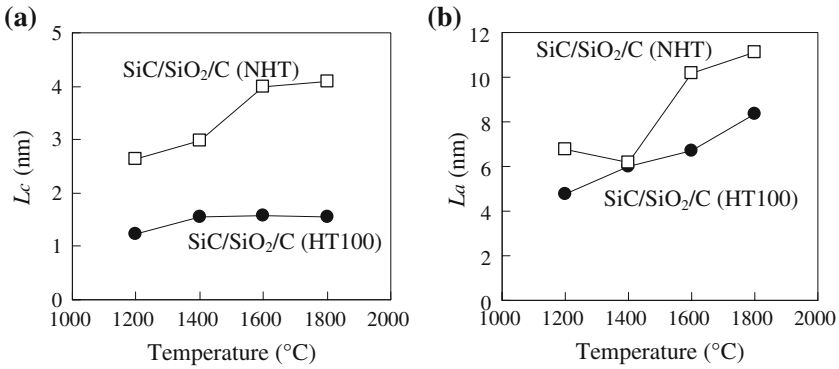

Fig. 2 **a** L_c and **b** L_a of carbon crystallites in porous SiC/SiO_2/C composites prepared by HT100 and NHT as a function of sintering temperature. *Solid circles* SiC/SiO_2/C (HT100), *open squares* SiC/SiO_2/C (NHT). *Note*: L_c height of the crystallite, L_a mean layer diameter. The meaning of SiC/SiO_2/C (HT100) and SiC/SiO_2/C(NHT) is the same as those in Fig. 1

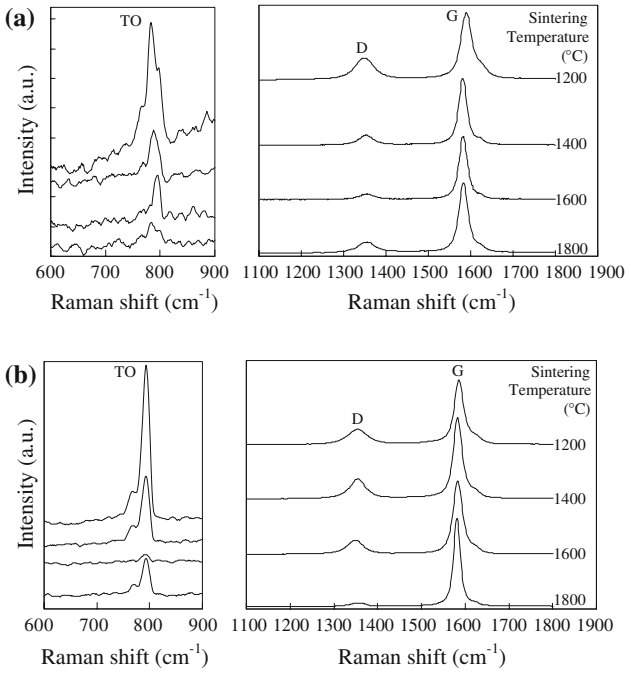

Fig. 3 Raman spectra in the ranges of 600–900 and 1100–1800 cm^{-1} of porous SiC/SiO_2/C composite prepared by **a** HT100 and **b** NHT at different sintering temperatures. *TO* transverse optic, *D* disorder, *G* graphite. The meaning of SiC/SiO_2/C (HT100) and SiC/SiO_2/C (NHT) is the same as those in Fig. 1

18]. A large TO peak was found at sintering temperature of 1200 °C both in the SiC/SiO_2/C (HT100) and SiC/SiO_2/C (NHT) samples indicating the formation of β-SiC. The FWHM of this peak, which provides information on the characteristics of the β-SiC crystals, is plotted against sintering temperature in Fig. 4a. For SiC/SiO_2/C (HT100), the FWHM decreases with increasing sintering temperature from 1200 to 1600 °C, and then increases from 1600 to 1800 °C. By contrast, for SiC/SiO_2/C (NHT), the FWHM decreases slightly as the sintering temperature is increased. Narrowing of the TO peak in SiC/SiO_2/C composites is related to ordering of the β-SiC crystals [17]. In the case of SiC/SiO_2/C (NHT), it is suggested that a solid–solid reaction occurred between SiO_2 and carbonized wood to form β-SiC during pulse current sintering due to the availability of SiO_2, resulting in a comparable amount of ordering of the β-SiC crystals in composites sintered at different temperatures. In the case of SiC/SiO_2/C (HT100), the gas–solid reaction of SiO and carbonized wood which produces β-SiC is difficult to control by this method, and β-SiC is formed with less ordering in the crystal structure.

Figure 3b shows the Raman spectra of SiC/SiO_2/C (HT100) and SiC/SiO_2/C (NHT), exhibiting broad D and G bands at around 1349–1357 and 1582–1589 cm^{-1}, respectively, attributed to carbon material with a turbostratic structure [1]. The D-band is associated with the disordered structure of turbostratic carbon while the G-band corresponds to crystallite vibration [19]. The FWHM of the D and G bands, as shown in Fig. 4b, c, corresponds to the degree of order in the carbon microstructure. Its value was found to be smaller for SiC/SiO_2/C (NHT) than for SiC/SiO_2/C (HT100), and in both cases decreased with increasing sintering temperature. Narrowing of the D- and G-band corresponds to an improvement in the carbon microstructure during sintering. As discussed previously, the HT100 and NHT pre-treatments gave rise to different phases of SiO_2 promoted by gas–solid and solid–solid reactions, respectively. A gas–solid reaction may cause infiltration of SiO gas into carbonized wood leading to less ordering of the carbon microstructure in addition to less growth of carbon crystallites, as was seen from the XRD analysis. On the other hand, a solid–solid reaction at the interface between SiO_2 and carbonized wood causes an increased amount of ordering of the carbon microstructure and larger carbon crystallites, leading to a good correlation between the Raman spectroscopy and XRD results.

Figure 5 shows the Si-2p spectra obtained by XPS analysis from SiC/SiO_2/C (HT100) and SiC/SiO_2/C (NHT) samples sintered at 1200, 1600, and 1800 °C, respectively. The Si-2p can be analyzed on the basis of a component at 100.8 eV that can be assigned to Si–C bonds and another component at 103.5 eV that can be assigned to Si–O bonds [20]. Thus XPS provides evidence of the concentration of

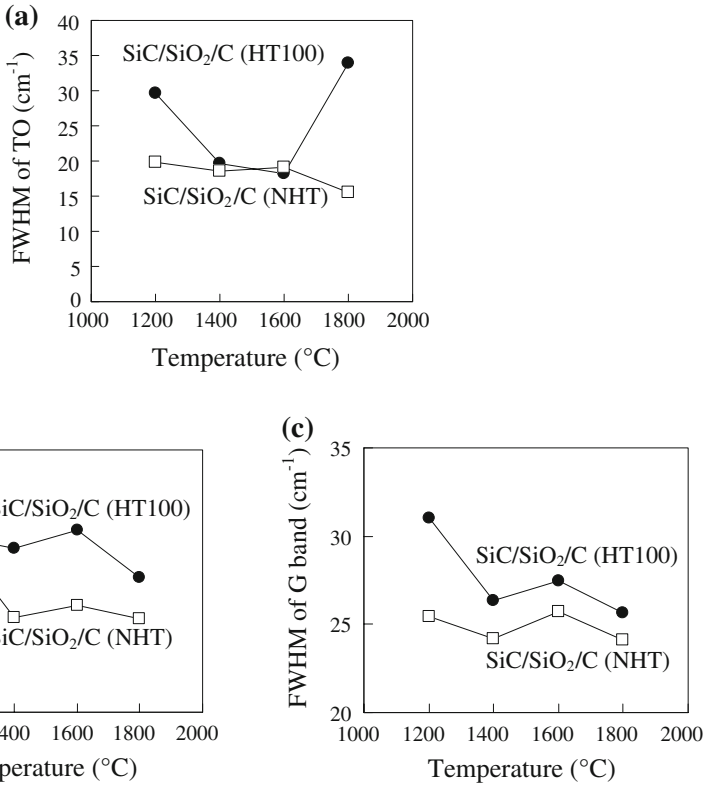

Fig. 4 FWHM of the **a** TO, **b** D, and **c** G bands of porous $SiC/SiO_2/C$ composites prepared by HT100 and NHT as a function of sintering temperature. *Solid circles* HT100, *open squares* NHT. The meaning of $SiC/SiO_2/C$ (HT100) and $SiC/SiO_2/C$ (NHT) is the same as those in Fig. 1

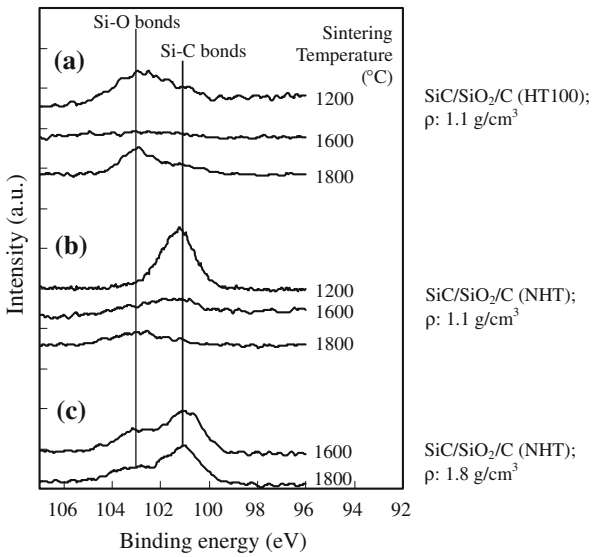

Fig. 5 Si-2p spectra of porous $SiC/SiO_2/C$ composite prepared by **a** HT100 and **b–c** NHT as a function of sintering temperature showing the peaks relevant to SiO_2 and SiC. The meaning of $SiC/SiO_2/C$ (HT100) and $SiC/SiO_2/C$ (NHT) is the same as those in Fig. 1

SiC and SiO_2 in the composite. The formation of β-SiC was most efficient at 1200 °C in $SiC/SiO_2/C$ (NHT) samples with a density of 1.1 g/cm^3 as shown in Fig. 5b. The same evidence was found by the strong TO peak in the Raman measurements for this sample, as shown in Fig. 3b. $SiC/SiO_2/C$ (NHT) samples with a density of 1.8 g/cm^3 prepared by applying an extra pressure of 15 MPa during sintering also showed the formation of β-SiC both on samples sintered at 1600 and 1800 °C, but to a lesser extent. Probably, the formation of β-SiC has been suppressed by this increase in pressure during sintering as result of an increased stability of silica and carbon [21]. A higher temperature is required to bring about the reaction between crystalline silica and carbon.

The results of the chemical bond analysis performed by XPS are put together in Table 1. As discussed previously, the Si–C bond in silicon carbide and the Si–O bond in silica (SiO_2) can be analyzed based on the Si-2p peak, while the C-1s peak can be analyzed into components corresponding to C–C or C–H, and four other components occurring at higher binding energy which can be assigned to C–O, C=O, O–C=O and the plasmon peak [20, 22]. The C–C bond was the main component on the C-1s peak that increased with temperature from 1200 to 1600 °C, then decreased to 1800 °C, except on the $SiC/SiO_2/C$ samples with a density of 1.8 g/cm^3. As discussed previously, at sintering temperature of 1200 °C β-SiC was more formed in the $SiC/SiO_2/C$ (NHT) sample, supported by the XPS result and the Raman spectroscopy.

Figure 6a, b shows SEM images of porous $SiC/SiO_2/C$ (HT100) and $SiC/SiO_2/C$ (NHT) sintered at different temperatures. In the case of $SiC/SiO_2/C$ (HT100), a large number of SiC rods exist inside the voids on the surface of

Table 1 Analysis of the chemical bonds of porous SiC/SiO_2/C composites from XPS experiments

Temperature (°C)	ρ (g/cm^3)	Si-2p (at.%)		C-1s (at.%)						O-1s (at.%)
		Si–C	Si–O	C–Si	C–C C–H	C–O C–OH	C=O	O–C=O	Plasmon	
Binding energy (eV)		100.8	103.5	282.4	284.6	285.7	289.1	289.3	292.3	
SiC/SiO_2/C(HT100)										
1200	1.1	4.6	6.6	30.1	33.2	8.8	2.5	7.5	2.9	3.8
1600	1.1	0.4	0.3	3.7	63.0	15.1	5.4	2.3	4.2	5.6
1800	1.1	0.5	0.2	2.5	53.2	19.5	8.6	2.2	6.7	6.5
SiC/SiO_2/C(NHT)										
1200	1.1	4.3	0.8	30.0	33.1	14.5	5.1	2.9	7.3	2.0
1600	1.1	1.4	0.8	5.7	59.9	12.1	4.0	1.8	8.3	6.1
1800	1.1	0.4	0.3	20.1	45.4	18.5	5.1	1.9	5.0	3.3
1600	1.8	0.8	1.4	17.9	40.7	3.6	23.2	2.3	3.3	6.8
1800	1.8	1.5	0.5	6.2	60.8	16.9	4.4	2.3	2.8	5.2

the carbonized wood particles, as indicated by arrow A in Fig. 6a. These rods were grown via a vapor–liquid–solid mechanism that has been discussed in previous papers [9, 12, 23]. During the sintering, chemical reactions occurred between gaseous SiO and CO providing transport for the carbon and silicon needed for the growth of the SiC rods. The SiO gas was produced by the reaction between SiO_2 (in liquid phase) and carbonized wood as discussed previously. In the case of SiC/SiO_2/C (NHT), spherical SiO_2 particles are distributed over the surface of the carbonized wood particles, as indicated by arrow B in Fig. 6b. It appears that during sintering at temperatures from 1200 to 1600 °C, the solid phase SiO_2 layer on the surface of carbonized wood particles melted to form spherical particles. In addition, reaction between the melted SiO_2 and carbonized wood to form β-SiC occurred at the interface area, in accordance with previous reports [6, 24].

The higher magnification SEM images seen in Fig. 7a, b clearly show the morphological differences between SiC/SiO_2/C (HT100) and SiC/SiO_2/C (NHT) samples. Since the reaction to form β-SiC is thought to involve SiO gas, a smooth surface of carbonized wood particles was found in the SiC/SiO_2/C (HT100) composite, as shown by arrow A in Fig. 7a. By contrast, thick, rough layers of β-SiC and SiO_2 covered the residual carbon in SiC/SiO_2/C (NHT), as shown in Fig. 7b. It is suggested that the SiO_2 layer that covered the carbonized wood melted and reacted with the wood at the interface to form β-SiC. In the case of samples sintered at temperatures in the range 1200–1600 °C, large amounts of SiO_2 solidified during the cooling and formed the thick, rough layers of SiO_2 reacting with carbonized wood to form β-SiC only at the interface. Morphology of the composite was changed at 1800 °C yielding a smoother surface as shown in Fig. 7b. The SEM result on the SiC/SiO_2/C (NHT) samples supported the XPS analysis that showed that less β-SiC formation occurred with the increase of sintering temperature, especially sintering at 1800 °C.

Figure 8 shows the TEM image of a SiC/SiO_2/C (HT100) sample sintered at 1600 °C, which reveals that β-SiC was formed in the interior of carbonized wood. The SiO gas that is produced from the reaction of SiO_2 (liquid) and carbonized wood, infiltrates into a carbonized wood particle and forms β-SiC.

Figure 9a, b shows higher magnification SEM images of SiC/SiO_2/C (NHT) with a density of 1.8 g/cm^3 (denoted as HD) sintered at 1600 and 1800 °C. The formation of β-SiC layers is difficult to distinguish in the HD sample sintered at 1600 °C, as shown in Fig. 9a. More obvious are the spherical SiO_2 particles distributed over the surface of carbonized wood. In the case of a HD sample sintered at 1800 °C, a thick layer of SiO_2 and β-SiC formed on the surface of carbonized wood, as shown in Fig. 9b. The formation of β-SiC could be detected only at the interface of SiO_2 and carbonized wood as discussed previously. The larger amount of β-SiC in HD samples sintered at 1800 °C supported the XPS analysis.

Figure 10a, b shows the electrical and thermal conductivities of SiC/SiO_2/C (HT100) and SiC/SiO_2/C (NHT) as a function of sintering temperature. The thermal conductivity (K_T) in semiconductor materials such as SiC/SiO_2/C composites can be decomposed into electron (K_e) and phonon (K_{ph}) components by using the Wiedemann–Franz law [25] as follows:

$$K_e = \frac{LT}{\rho} \tag{3}$$

where L is the Lorenz number, T is the temperature, and ρ the electrical resistivity. The Lorenz number was assumed to be a universal constant of 2.45×10^{-8} W Ω/K^2. Based

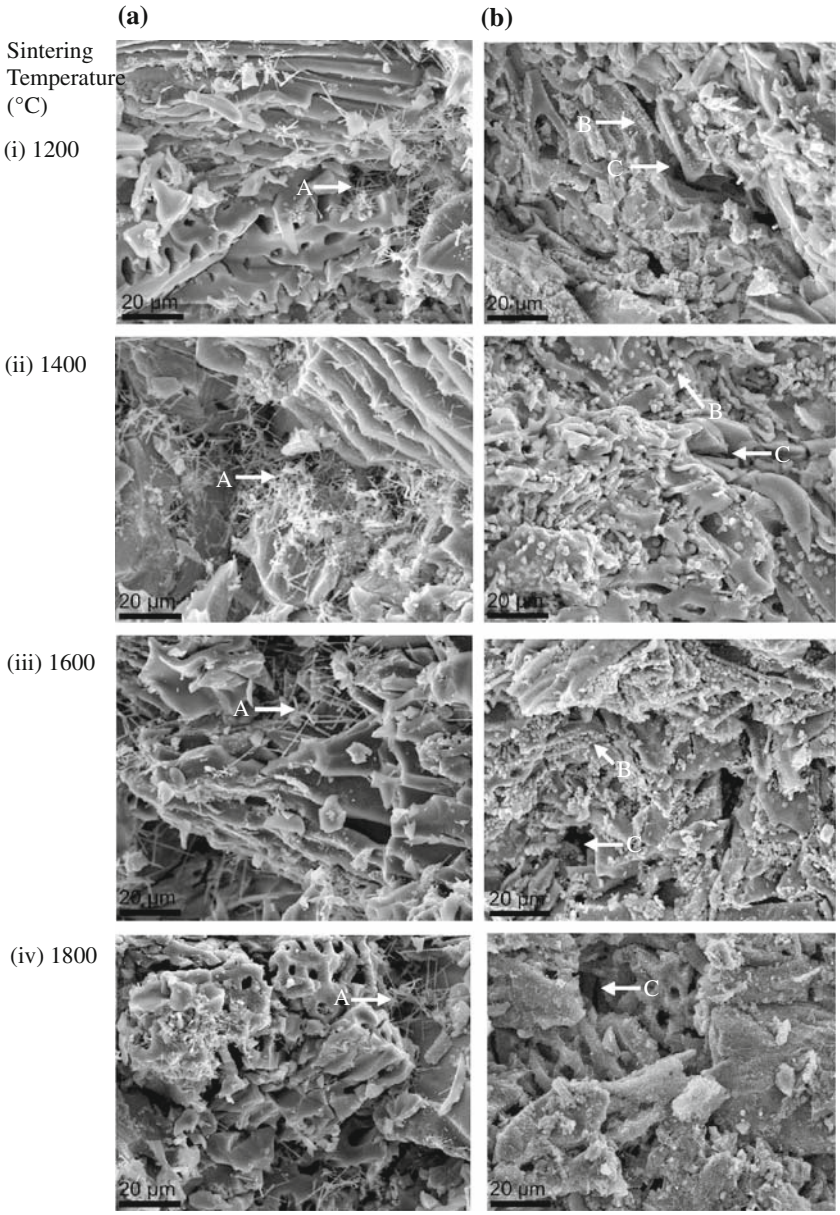

Fig. 6 SEM images of porous $SiC/SiO_2/C$ composites prepared by **a** HT100, exhibiting SiC rods (*arrow A*) grown on the surface of carbonized wood particles and **b** NHT, exhibiting SiO_2 spherical particles (*arrow B*) spread over the surface of carbonized wood particles and empty voids (*arrow C*), at different sintering temperatures. The meaning of $SiC/SiO_2/C$ (HT100) and $SiC/SiO_2/C$ (NHT) is the same as those in Fig. 1

on this equation, the phonon component was predominant in the thermal conductivity of the porous $SiC/SiO_2/C$ composites used in this study. Both electrical and thermal conductivities increased with sintering temperature due to an increase in the degree of structural ordering of the β-SiC crystals [26] and carbon crystallites in carbonized wood [27]. The effect of β-SiC on the electrical conductivity appears to be similar to that seen in a previous study where a porous SiC composite with a high electrical conductivity of $2.5 \times 10^4\ \Omega^{-1}\ m^{-1}$ was reported [28]. The electrical conductivity of $SiC/SiO_2/C$ (NHT) sintered at temperatures in the range 1200–1600 °C was much lower than that of $SiC/SiO_2/C$ (HT100), which possessed less β-SiC and had a lower degree of ordering. This was due to the existence of a thick SiO_2 layer, which is electrically insulating [29]. The higher electrical and thermal conductivities of $1.17 \times 10^4\ \Omega^{-1}\ m^{-1}$ and 25 W/mK were obtained for $SiC/SiO_2/C$ (NHT) sintered at 1800 °C, due to the greater size of carbon crystallites, the higher degree of ordering of the microstructure of carbon and β-SiC crystals, and the smaller amount of SiO_2. In contrast, the thermal conductivity of $SiC/SiO_2/C$ (HT100) exhibited a very low value of only 2 W/mK at 1600 °C, due to the lesser crystallinity of carbon and β-SiC.

Figure 11a, b shows the electrical and thermal conductivities of $SiC/SiO_2/C$(NHT) sintered at 1600 and 1800 °C as a function of density. A maximum value of $1.5 \times 10^4\ \Omega^{-1}\ m^{-1}$ and 101 W/mK were recorded for the

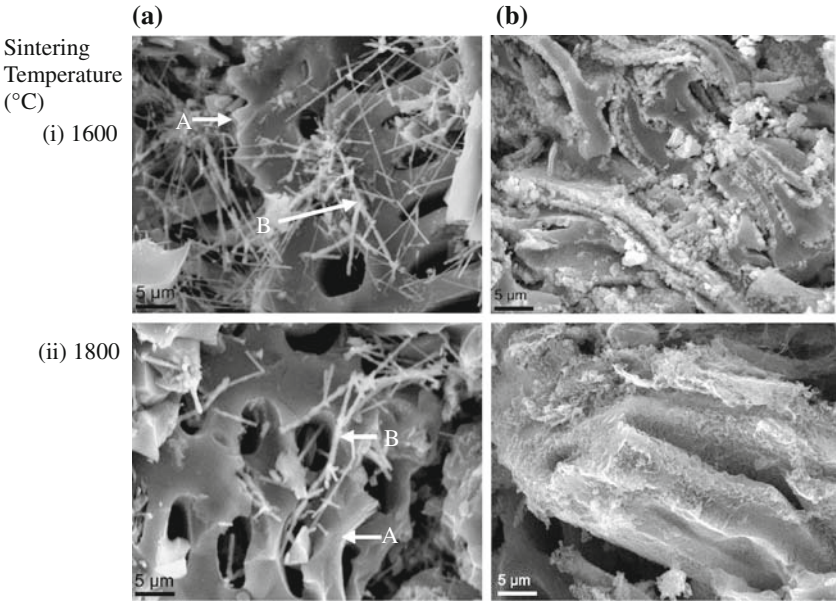

Fig. 7 Higher magnification SEM images showing different type of β-SiC in porous SiC/SiO_2/C composites prepared by **a** HT100, exhibiting smooth surface (*arrow A*) and SiC rods (*arrow B*) grown on carbonized wood surface; and **b** NHT, exhibiting rough surface β-SiC layer on carbonized wood particles. The meaning of SiC/SiO_2/C (HT100) and SiC/SiO_2/C (NHT) is the same as those in Fig. 1

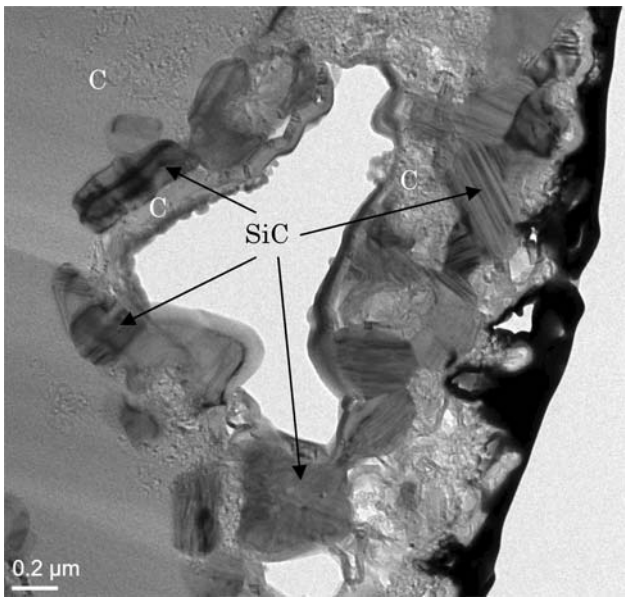

Fig. 8 TEM image of SiC/SiO_2/C (HT100) composite sintered at 1600 °C

composite prepared at 1800 °C with a density of 1.82 g/cm^3. The electrical and thermal conductivities of this sample increased as a result of a greater amount of well-ordered β-SiC indicated by the narrow TO peak with a width of 14 nm, growth of carbon crystallites with $L_a = 19$ nm and $L_c = 11$ nm, and higher ordering of the carbon microstructure. However, in the case of SiC/SiO_2/C (NHT) sintered at 1600 °C a lesser formation of β-SiC and a larger content of SiO_2 occurred as shown by XPS analysis in Table 1 and more or less confirmed by the SEM image in Fig. 9a. This leads to a lesser electrical conductivity.

Conclusions

Porous SiC/SiO_2/C composites with a wide range of electrical and thermal conductivity were prepared using different pre-treatments followed by sintering at various temperatures. Pre-treatment leading to carbonized wood infiltrated with SiO_2 at room temperature followed by sintering at 1800 °C produced porous SiC/SiO_2/C composites with high electrical and thermal conductivities of $1.17 \times 10^4\ \Omega^{-1}\ m^{-1}$ and 25 W/mK, respectively. The thermal conductivity could be improved to 101 W/mK by increasing the density of the composite to 1.82 g/cm^3. Pre-treatment leading to carbonized wood infiltrated with SiO_2 at 100 °C followed by sintering at temperatures in the range 1200–1800 °C generated porous SiC/SiO_2/C composites possessing a high electrical conductivity of $1 \times 10^4\ \Omega^{-1}\ m^{-1}$, but a low thermal conductivity of 2 W/mK due to the reduced amount of β-SiC within the composite.

In summary, porous SiC/SiO_2/C composites with a wide range of thermal conductivity from 0.9 to 101 W/mK and a range of high electrical conductivity of 6×10^3–$2 \times 10^4\ \Omega^{-1}\ m^{-1}$ were developed from carbonized wood. Such high thermal conductivity composites are preferable for effective thermal management in SPS. In the SPS, the thermal management is required to release heat from solar panels and microwave transmitter [30]. SiC/SiO_2/C(NHT)

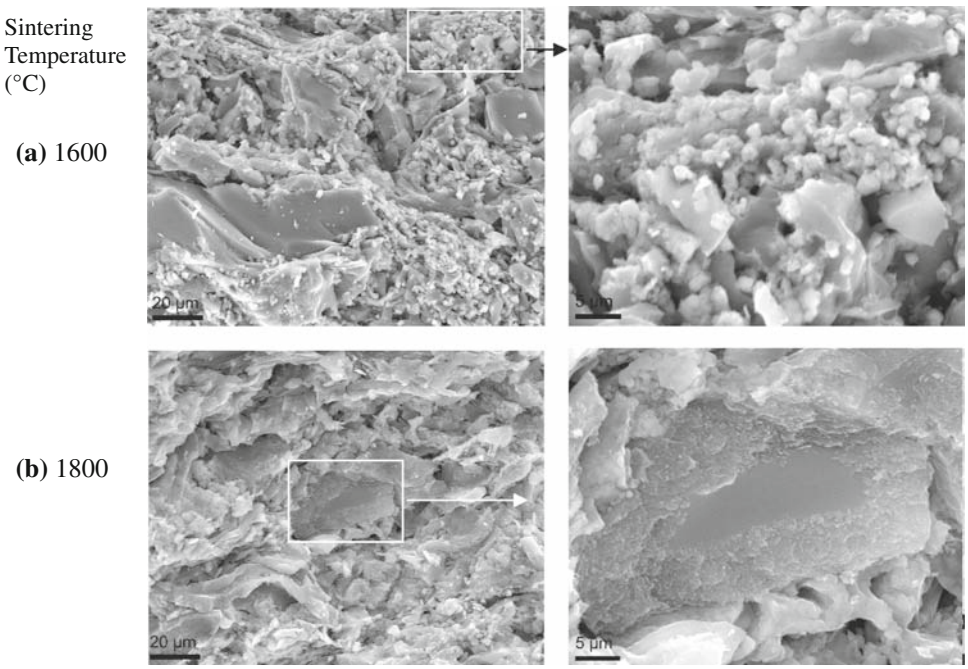

Fig. 9 SEM images of porous $SiC/SiO_2/C$ (NHT) composites with density of 1.8 g/cm^3 prepared at **a** 1600 °C exhibiting a large number of spherical SiO_2 particles on the surface of carbonized wood particles and **b** at 1800 °C. The *right images* are the higher magnification of the square areas in the *left images*. The meaning of $SiC/SiO_2/C$ (NHT) is the same as that in Fig. 1

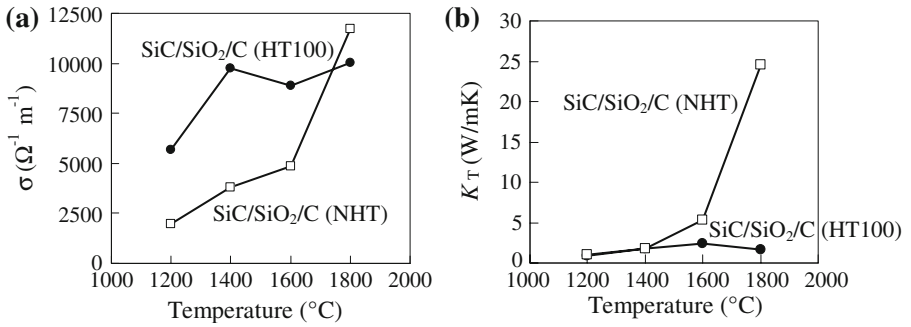

Fig. 10 **a** Electrical and **b** thermal conductivities of porous $SiC/SiO_2/C$ composites prepared by HT100 and NHT as a function of sintering temperature. *Solid circles* $SiC/SiO_2/C$ (HT100), *open squares* $SiC/SiO_2/C$ (NHT). The meaning of $SiC/SiO_2/C$ (HT100) and $SiC/SiO_2/C$ (NHT) is the same as those in Fig. 1

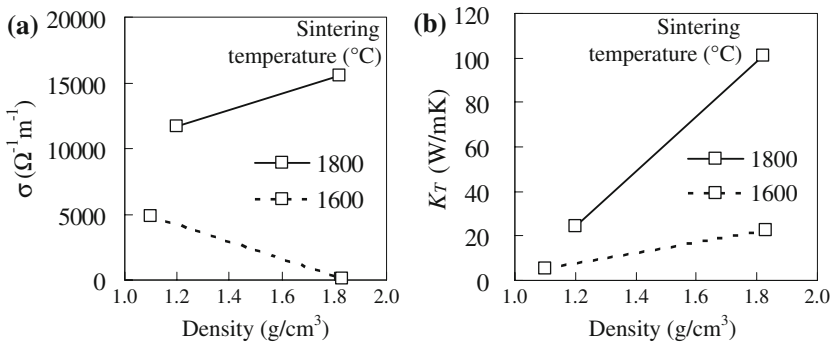

Fig. 11 **a** Electrical and **b** thermal conductivities of porous $SiC/SiO_2/C$ (NHT) composites as a function of density

prepared at 1800 °C will be applicable as thermal conductive material by controlling the direction of heat flow.

References

1. Ishimaru K, Hata T, Bronsveld P, Imamura Y (2007) J Mater Sci 42:2662. doi:10.1007/s10853-006-1361-4
2. Rodriguez-Reinoso F, Molina-Sabio M (1992) Carbon 30:1111
3. Greil P (2001) J Eur Ceram Soc 21:105
4. Fujisawa M, Hata T, Bronsveld P, Castro V, Tanaka F, Kikuchi H, Furuno T, Imamura Y (2004) J Eur Ceram Soc 24:3575
5. Vogli E, Sieber H, Greil P (2002) J Eur Ceram Soc 22:2663
6. Varela-Feria FM, Ramirez-Rico J, de Arellano-Lopez AR, Martinez-Fernandez J, Singh M (2008) J Mater Sci 43:933. doi:10.1007/s10853-007-2207-4
7. Greil P (2002) Adv Eng Mater 4:247
8. Shiryaev AA, Wiedenbeck M, Reutsky V, Polyakov VB, Melnik NN, Lebedev AA, Yakimova R (2008) J Phys Chem Solids 69:2492

9. Cheung TLY, Ng DHL (2007) J Am Ceram Soc 90:559
10. Klett JW, McMillan AD, Gallego NC, Walls CA (2004) J Mater Sci 39:3659. doi:10.1023/B:JMSC.0000030719.80262.f8
11. Warren BE (1941) Phys Rev 59:693
12. Vyshnyakova K, Yushin G, Pereselentseva L, Gogotsi Y (2006) Int J Appl Ceram Technol 3:485
13. Lu Q, Hu J, Tang K, Qian Y, Zhou G, Liu X, Zhu J (1999) Appl Phys Lett 75:507
14. Li ZQ, Lu CJ, Xia ZP, Zhou Y, Luo Z (2007) Carbon 45:1686
15. Kuomoto K, Takeda S, Pai CH, Sato T, Yanagida H (1989) J Am Ceram Soc 72:1985
16. Kercher AK, Nagle DC (2003) Carbon 41:15
17. Nakashima S, Harima H (1997) Phys Status Solidi (a) 162:39
18. Rohmfeld S, Hundhausen S, Ley L (1999) Phys Status Solidi (b) 215:115
19. Cuesta A, Dhamelincourt P, Laureyns J, Martinez-Alonso A, Tascon JMD (1994) Carbon 32:1523
20. Bouillon E, Langlais F, Pailler R, Naslain R, Cruege F, Huong PV, Sarthou JC, Delpuech A, Laffon C, Lagarde P, Monthioux M, Oberlin A (1991) J Mater Sci 26:1333. doi:10.1007/BF00544474
21. Krishnarao RV, Mahajan YR (1996) Ceram Int 22:353
22. Miyagawa S, Baba K, Ikeyama M, Saitoh K, Nakao S, Miyagawa Y (1997) Nucl Instrum Methods Phys Res B 127/128:651
23. Hata T, Castro V, Fujisawa M, Imamura Y, Bonnamy S, Bronsveld P, Kikuchi H (2005) Fuller Nanotube Carbon Nanostruct 13:107
24. Zollfrank C, Sieber H (2005) J Am Ceram Soc 88:51
25. Parfeneva LS, Orlova TS, Kartenko NF, Sharenkova NV, Smirnov BI, Smirnov IA, Misiorek H, Jezowski A, Mucha J, de Arellano-Lopez AR, Martinez-Fernandez J, Varela-Feria FM (2006) Phys Solid State 48:441
26. Chung DDL (2002) J Mater Sci 37:1475. doi:10.1023/A:1014915307738
27. Xie X, Goodell B, Qian Y, Peterson M, Jellison J (2008) Holzforschung 62:591
28. Orlova TS, Smirnov BI, de Arellano-Lopez AR, Martinez Fernandez J, Sepulveda R (2005) Phys Solid State 47:229
29. Ito M, Tanaka T, Hara S (2004) J Appl Phys 95:6209
30. Fujita T, Saito Y, Yoshida H, Masahiro M (2006) In: Proceedings of the 3rd International Symposium on Sustainable Energy System 2006, Kyoto